

Cite this: *Dalton Trans.*, 2021, **50**, 7995

Single-atom Fe–N₄ site for the hydrogenation of nitrobenzene: theoretical and experimental studies†

Yan Liu,^a Wenzhuang Zhang,^a Yamin Zheng,^a Konglin Wu,^b Panpan Dong,^a Rong He,^c Ning Lu^a and Junjie Mao^{*a}

The hydrogenation of nitrobenzene to aniline is an important process in the industry of fine chemicals, but developing inexpensive catalysts with expected activity and selectivity still remains a challenge. By using density functional theory calculations, we demonstrated that the isolated Fe atom not only can weaken the adsorption of reactants and reaction intermediates as compared to Fe nanoparticles, but also remarkably decrease the reaction barrier for the hydrogenation of nitrobenzene to aniline. Thus, the Fe single-atom (Fe SA) catalyst is considered as an ideal catalyst for this reaction. This theoretical prediction has been subsequently confirmed by experimental results obtained for the Fe SAs loaded on N-doped hollow carbon spheres (Fe SAs/NHCSSs) which achieved a conversion of 99% with a selectivity of 99% for the hydrogenation of nitrobenzene. The results significantly outperformed the Fe nanoparticles for this reaction. This work provides theoretical insight for the rational design of new catalytic systems with excellent catalytic properties.

Received 14th April 2021,
Accepted 6th May 2021

DOI: 10.1039/d1dt01227d

rsc.li/dalton

Introduction

As an important raw material in the industry of fine chemicals, aniline is widely used for the production of pesticides, medicines, polymeric surfactants, and dyes.^{1–5} In the production of aniline, the catalytic hydrogenation of nitrobenzene is the commonly used synthetic strategy. Noble metal-based catalysts, such as Pt, Pd, and Ru, are highly active for the hydrogenation reaction.^{6–10} For example, Li and co-workers demonstrated that corroded PtNi₃ alloy showed high catalytic activity and selectivity towards the hydrogenation of nitrobenzene.¹⁰ However, the scarcity and high cost of noble metal-based catalysts hamper their practical use. Moreover, the hydrogenation of nitrobenzene to aniline is complex, involving several parallel and cascade reactions that cause the formation of by-products, such as hydroxylamine and azo-compounds. The intermediate products show poor selectivity over the commonly used noble

metal catalysts. The composite structure of catalysts can also be used in the hydrogenation reaction. For example, Xiao *et al.* reported that the Au/Sn-TiO₂ catalyst exhibited high catalytic activity in the hydrogenation of nitroarenes.¹¹ However, the complex nanostructure/nanointerface is not conducive to the understanding of the catalytic active center and also brings difficulties to the deeper mechanistic research. In this regard, it is highly desired to develop inexpensive catalysts with well-defined catalytic structure and adequate activity and selectivity for the conversion of nitrobenzene to aniline. Single atom (SA) catalysts with the highest atomic utilization and a unique electronic structure have received considerable attention recently.^{12–35} For example, Wang and co-workers developed a series of synthetic strategies for preparing SAs with various applications including electrocatalysis, photocatalysis and organic catalysis,^{36,37} providing great opportunities for achieving high performance catalysts toward industrial applications.

In this study, we demonstrated, by means of systematic theoretical analysis, that Fe single atoms (Fe SAs) are ideal catalysts for the hydrogenation of nitrobenzene. Specifically, we simulated all the possible reaction pathways of the hydrogenation of nitrobenzene over Fe SAs and Fe nanoparticles (Fe NPs). Density functional theory (DFT) calculations showed that adsorption of nitrobenzene and reaction intermediates on Fe SAs is not only weaker than that on Fe NPs, but these SAs largely decreased the energy barrier of the hydrogenation reaction. To confirm the theoretical prediction, we synthesized the

^aKey Laboratory of Functional Molecular Solids, Ministry of Education, Anhui Province Key Laboratory of Optoelectric Materials Science and Technology and Anhui Laboratory of Molecule-Based Materials, Anhui Normal University, Wuhu, 241002, China. E-mail: maochem@ahnu.edu.cn

^bSchool of Chemistry and Chemical Engineering, Anhui University of Technology, Maanshan 243002, China

^cState Key Laboratory of Environment-friendly Energy Materials, Southwest University of Science and Technology, Mianyang, 621010, China

†Electronic supplementary information (ESI) available. See DOI: 10.1039/d1dt01227d

Fe single atoms on the N-doped hollow carbon spheres (Fe SAs/NHCSSs) and used them for the catalytic hydrogenation of nitrobenzene. Notably, Fe SAs/NHCSSs exhibited a conversion of nitrobenzene of 99% with a selectivity to aniline of 99%, which considerably outperformed Fe NPs/NHCSSs. The successful development of Fe SAs/NHCSSs as hydrogenation catalysts is a prototype for the rational design of catalytic systems at the atomic level based on the theoretical calculation.

Results and discussion

To investigate the stable structure of the Fe SA catalyst, geometry optimizations of all possible adsorption configurations of a single Fe atom on the graphene were performed, and the corresponding binding energies were calculated (ESI, Fig. S1†). As shown in Fig. 1a, a single Fe atom coordinated with four N atoms (FeN_4) can be strongly adsorbed on graphene, with a binding energy of 6.51 eV. The difference charge density shown in Fig. 1b reveals the electronic structure of a single Fe atom coordinated with N. Therefore, we selected the FeN_4 structure as a model to study the mechanism of the hydrogenation of nitrobenzene to aniline on the surface of the Fe SA catalyst. Because the adsorption of reactants plays an important role in the heterogeneous catalytic reactions, we first simulated the possible adsorption configurations of nitrobenzene on the FeN_4 structure. The adsorption configurations of nitrobenzene were classified into two types, *i.e.*, vertical and parallel adsorption. All the optimized structures and adsorption energies of these configurations are displayed in ESI, Fig. S2.† The adsorption energy of the parallel configuration (0.65 eV) was higher than that of the vertical adsorption configuration (0.30 eV). Accordingly, it can be stated that nitrobenzene prefers to adsorb on the surface of the Fe SA catalyst in the parallel mode (Fig. 1c). Afterwards, we simulated the difference charge of the parallel adsorption configuration (Fig. 1d). The significant charge transfer between the nitro group of nitrobenzene and Fe atom suggests a strong inter-

action between the reactant and FeN_4 catalyst, which is favorable for the reaction.

To further evaluate the catalytic activity of the Fe SA catalyst, we simulated all possible reaction pathways of the nitrobenzene hydrogenation reaction. As shown in ESI, Scheme S1,† four hydrogenation pathways of nitrobenzene to aniline are possible.^{38,39} The common features of them must undergo the dissociation of N–O bonds and the formation of N–H (O–H) bonds, whereas the difference between them is whether the N–O bond dissociation occurs first during the second and fourth steps of the hydrogenation reaction. To identify the optimal reaction path, we calculated the reaction energies and the activation energies of all the corresponding elementary steps (ESI, Table S1†). Fig. 2 displays the energy profiles of all the reaction pathways, and the optimal reaction pathway is shown with a red line. The first step of all these routes is the transfer of the H atom to the O atom of the nitro group to form an O–H bond and generate $\text{C}_6\text{H}_5\text{NOOH}$, a process needing to overcome an energy barrier of 0.60 eV. In the second step, two competitive pathways exist. One was the hydrogenation of $\text{C}_6\text{H}_5\text{NOOH}$ to form $\text{C}_6\text{H}_5\text{N}(\text{OH})_2$, whereas the other corresponds to the dissociation of N–O bonds in $\text{C}_6\text{H}_5\text{NOOH}$ to form $\text{C}_6\text{H}_5\text{NO}$. The formation of $\text{C}_6\text{H}_5\text{N}(\text{OH})_2$ is an exothermic process and releases an energy of 1.61 eV. However, the activation barrier of the subsequent dehydroxylation to $\text{C}_6\text{H}_5\text{NOH}$ (0.89 eV) is 0.22 eV higher than that of the formation of $\text{C}_6\text{H}_5\text{NO}$ (0.67 eV). Thus, it is more likely that the dissociation of the N–O bond occurs for the production of $\text{C}_6\text{H}_5\text{NO}$. Next, the formation of $\text{C}_6\text{H}_5\text{NOH}$ requires a barrier of 0.02 eV, while it releases an energy of 1.27 eV. Unlike the second step of the hydrogenation reaction, the H atom in the hydrogenation process of $\text{C}_6\text{H}_5\text{NOH}$ prefers to bind with N to form an N–H bond, which is easier than the dissociation of the N–O bond in $\text{C}_6\text{H}_5\text{NOH}$. The activation energy of 0.87 eV for the fifth step is the highest, which makes it the rate-determining step of the whole reaction process. In this step, an alternative pathway of the five-membered ring transition state for N–O bond cleavage was also investigated (ESI, Fig. S3†). This alternative pathway exhibited similar adsorption energy and activation energy to the original pathway in Fig. 2. Finally, H easily transfers to N to form $\text{C}_6\text{H}_5\text{NH}_2$ *via* an exothermic process, releasing an energy of 2.57 eV. Thus, the reaction mechanism on the Fe SA catalyst involves several consecutive reactions, which follow the order of $\text{C}_6\text{H}_5\text{NO}_2 \rightarrow \text{C}_6\text{H}_5\text{NOOH} \rightarrow \text{C}_6\text{H}_5\text{NO} \rightarrow \text{C}_6\text{H}_5\text{NOH} \rightarrow \text{C}_6\text{H}_5\text{NHOH} \rightarrow \text{C}_6\text{H}_5\text{NH} \rightarrow \text{C}_6\text{H}_5\text{NH}_2$.

For comparison, we also investigated the hydrogenation reaction pathway of nitrobenzene on the surface of the Fe NP catalyst. The energy profiles for all the hydrogenation reaction pathways on the Fe NP catalyst are shown in Fig. 3, while the corresponding activation and reaction energies are summarized in ESI, Table S2.† First, a stable Fe_6 configuration was used to simulate Fe NPs, as previously reported.⁴⁰ The calculated configuration of nitrobenzene and adsorption energies on the Fe NP catalyst are depicted in ESI, Fig. S4.† As noticed, the most stable adsorption mode of nitrobenzene was the parallel adsorption configuration, which was similar to that found

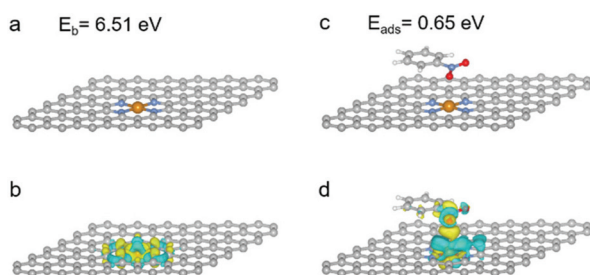


Fig. 1 (a) The optimized geometry and the binding energy of the FeN_4 structure. (b) Difference charge density of the FeN_4 structure. (c) The optimized geometry and the adsorption energy of $\text{C}_6\text{H}_5\text{NO}_2$ on the FeN_4 surface. (d) Difference charge density of the FeN_4 structure with the adsorption of nitrobenzene. C, N, O, H and Fe atoms are represented by grey, blue, red, white, and orange balls, respectively. The positive and negative changes are shown in yellow and cyan, respectively.

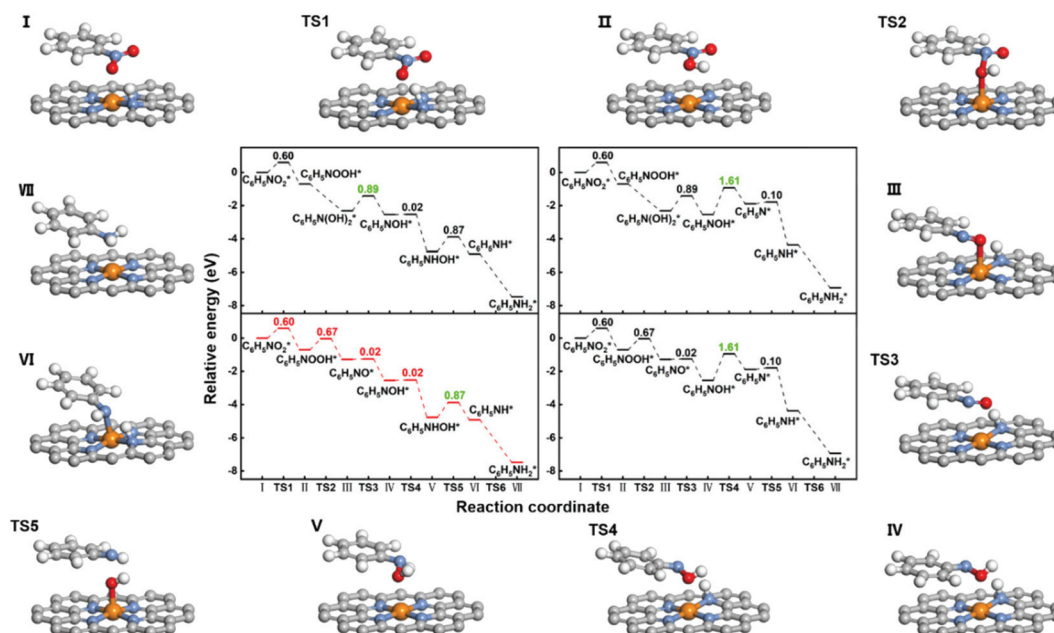


Fig. 2 Energy profiles of four possible reaction pathways for the hydrogenation of nitrobenzene to aniline on the FeN_4 structure. The red route represents the optimal reaction pathway. The green numbers represent the energy barriers of the rate-determining steps for the whole reaction process. Optimized structures of the intermediates and transition states for the optimal reaction pathway are exemplified.

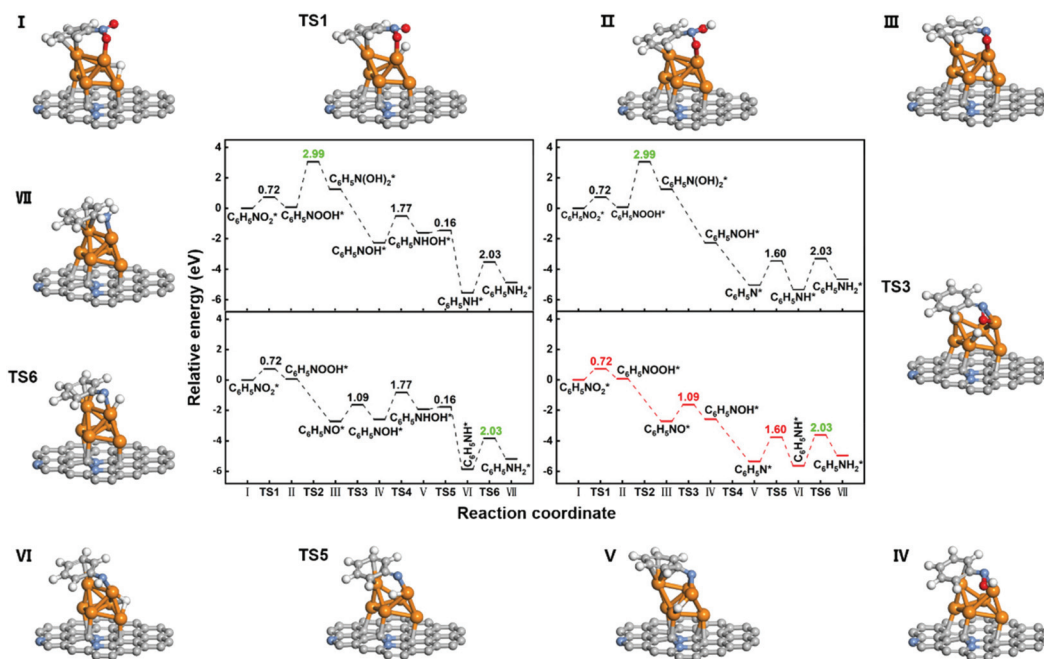


Fig. 3 Energy profiles of four possible reaction pathways for the hydrogenation of nitrobenzene to aniline on the Fe nanoparticles. The red route represents the optimal reaction pathway. The green numbers represent the energy barriers of the rate-determining steps for the whole reaction process. Optimized structures of the intermediates and transition states for the optimal reaction pathway are exemplified.

for Fe SAs. The adsorption energy between the reactant and catalyst is as high as 2.25 eV, implying a difficult occurrence of the subsequent hydrogenation reaction (ESI, Table S3†). In the light of calculation results, the optimal reaction pathway on the Fe NPs is different from that on the Fe SA catalyst, and it is

$\text{C}_6\text{H}_5\text{NO}_2 \rightarrow \text{C}_6\text{H}_5\text{NOOH} \rightarrow \text{C}_6\text{H}_5\text{NO} \rightarrow \text{C}_6\text{H}_5\text{NOH} \rightarrow \text{C}_6\text{H}_5\text{N} \rightarrow \text{C}_6\text{H}_5\text{NH} \rightarrow \text{C}_6\text{H}_5\text{NH}_2$. The hydrogenation of $\text{C}_6\text{H}_5\text{NH}$ to $\text{C}_6\text{H}_5\text{NH}_2$ is the rate-determining step of the whole process, with a barrier of 2.03 eV, and a reaction energy endothermic by 0.68 eV. Obviously, the hydrogenation reaction of nitrobenzene

on the Fe NP catalyst has to overcome a higher energy barrier than that on the Fe SA catalyst. Therefore, the above results prove that the Fe SA catalyst is a better catalyst for this hydrogenation reaction.

To verify the theoretical results, we performed the experimental studies on Fe SAs and Fe NPs. The typical synthetic strategy of Fe SAs/NHCSs is illustrated in Fig. 4a. First, polystyrene (PS) nanospheres were prepared *via* a previously reported procedure and used as the template. The PS template was then uniformly dispersed in an aqueous solution containing *m*-aminophenol and $\text{Fe}(\text{NO}_3)_3 \cdot 9\text{H}_2\text{O}$. After that, formaldehyde was injected into the mixture to obtain the PS@Fe(III)-aminophenol formaldehyde (APFR) product through condensation polymerization. In this case, the PS@Fe(III)-APFR retained the amino groups ($-\text{NH}_2$) of the *m*-aminophenol precursor, which served as the coordination sites for Fe^{3+} ions. The as-prepared PS@Fe(III)-APFR was finally carbonized under an Ar atmosphere to remove the PS template and form Fe SAs/NHCSs.

The precursor (PS@Fe(III)-APFR) and final sample (Fe SAs/NHCSs) were characterized in relation to their composition, morphology, and structure. The chemical compositions of Fe SAs/NHCSs determined by inductively coupled plasma mass spectrometry (ICP-MS) show that the weight percentage of Fe element in Fe SAs/NHCSs was 0.95%. The morphology was assessed by transmission electron microscopy (TEM) in comparison with that of pure PS. As shown in ESI, Fig. S5,† the PS template displays a sphere-like morphology with a homogeneous size distribution. As shown in Fig. 4b, the PS@Fe(III)-APFR precursor displays a similar morphology to the PS template, indicating the morphology preservation during the polymerization process. For Fe SAs/NHCSs, the decomposition of the PS template led to a hollow sphere-like morphology with spheres of an average diameter of *ca.* 250 nm (Fig. 4c). The TEM image of an individual hollow sphere of Fe SAs/NHCSs shows that the shell thickness of the carbon layer is 10 nm (Fig. 4d). As revealed by the results of N_2 adsorption and desorption experiments, Fe SAs/NHCSs display a high specific

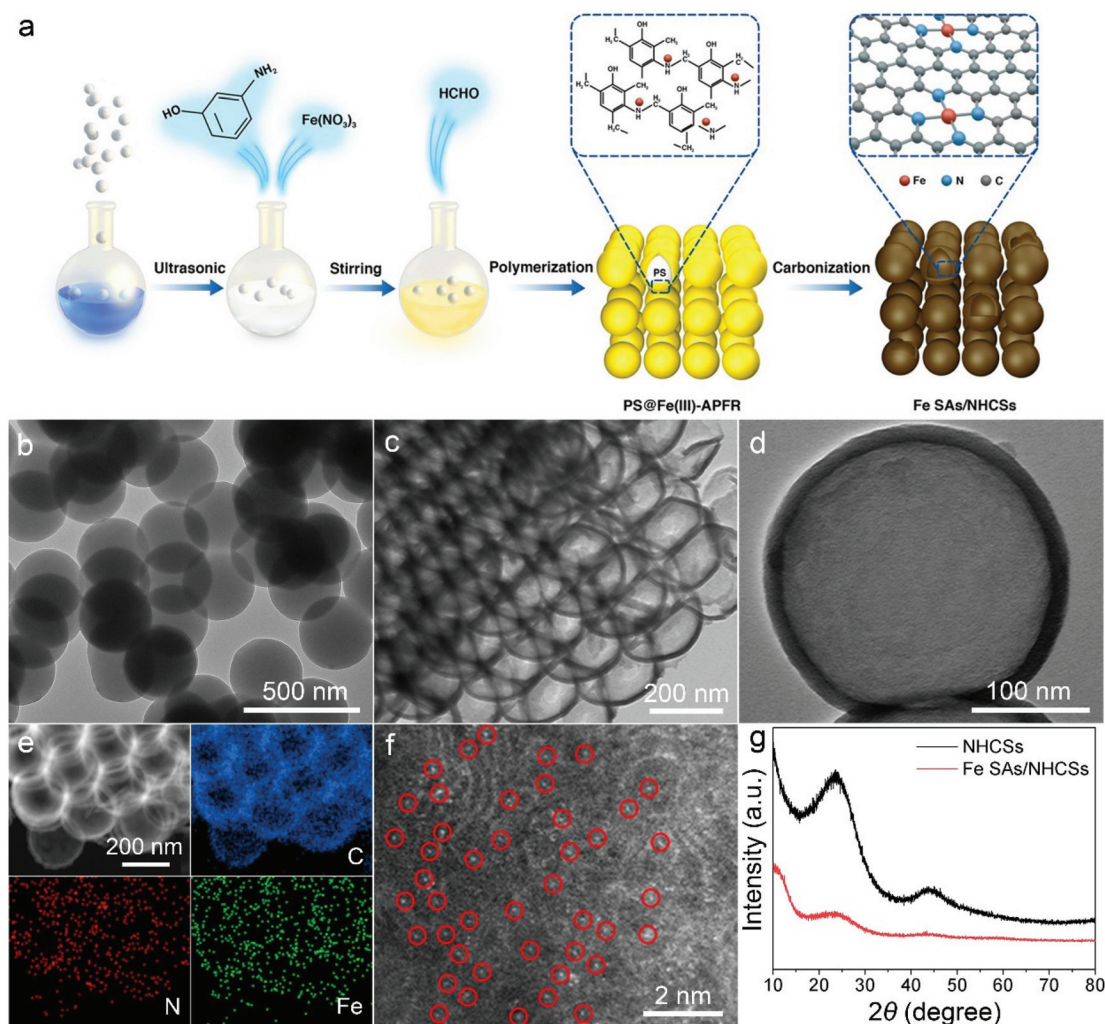


Fig. 4 (a) Schematic illustration of the synthesis of Fe SAs/NHCSs. (b) TEM images of PS@Fe(III)-APFR. (c) TEM images. (d) Magnified TEM images of the Fe SAs/NHCSs. (e) HAADF-STEM image and the corresponding EDX maps of Fe SAs/NHCSs. (f) Representative AC HAADF-STEM image of the Fe SAs/NHCSs. The red circles were drawn around the isolated Fe atom. (g) XRD pattern of Fe SAs/NHCSs and NHCSs.

area of $112 \text{ m}^2 \text{ g}^{-1}$ with a micropore size of 1.95 nm (ESI, Fig. S6†). Fig. 4e shows the high-angle annular dark field scanning transmission electron microscopy (HAADF-STEM) image and the corresponding energy dispersive X-ray (EDX) elemental mapping of the selected area for Fe SAs/NHCSSs. The C, N, and Fe elements are homogeneously distributed on the whole hollow sphere. The existence of these elements on the surface was further confirmed by XPS (ESI, Fig. S7†). The high resolution N 1s XPS spectrum displays signals at 398.4 eV, 400.2 eV and 401.2 eV, proving the co-existence of the pyridinic N, pyrrolic N, and graphitic N in Fe SAs/NHCSSs (ESI, Fig. S8(a)†). In addition, the Fe 2p XPS spectrum of Fe SAs/NHCSSs indicates a mixed valence of +2 and +3 (ESI, Fig. S8(b)†). The existing form of Fe was validated by the atomic-resolved HAADF-STEM image. Based on the heavier Z-contrast of Fe relative to N and C, the isolated Fe atoms were recorded in the carbon layer in the single-atom state (Fig. 4f). As shown in Fig. 4g, the XRD pattern of Fe SAs/NHCSSs does not display the characteristic peaks of iron, which exclude the existence of Fe NPs.

To explore the valence state and coordination environment of Fe species in Fe SAs/NHCSSs, we carried out X-ray absorption near edge structure (XANES) and extended X-ray absorption fine structure (EXAFS) experiments of Fe SAs/NHCSSs, Fe foil, and Fe_2O_3 . As shown in Fig. 5a, displaying the XANES spectra, the energy absorption edge of Fe SAs/NHCSSs is located between that of Fe foil and Fe_2O_3 , which indicates that the valence state of the Fe atom in Fe SAs/NHCSSs is between 0 and

+3. The EXAFS spectrum of Fe SAs/NHCSSs displays a single peak at 1.5 \AA , which corresponds to the Fe–N bond (Fig. 5b). Furthermore, no typical peak of Fe–Fe bonds with an interatomic distance of above 2.2 \AA could be found, demonstrating the atomically dispersed Fe species in the N-doped hollow carbon sphere. In addition, we performed a wavelet transform (WT) to further illustrate the Fe K-edge EXAFS oscillation (Fig. 5c). Only one intensity maximum at around 3.6 \AA^{-1} corresponding to the Fe–N bond was observed in the WT contour plot of Fe SAs/NHCSSs, which further confirms the isolation of Fe atoms in Fe SAs/NHCSSs. The chemical environment and the corresponding structural parameters of Fe atoms were determined by quantitative EXAFS fitting in the R space, k space and q space (Fig. 5d, e, and ESI, Fig. S9†). As shown in ESI, Table S4,† Fe SAs/NHCSSs exhibited a coordination number of 4.35 with an average bond length of 2.02 \AA , which shows that the Fe atom in Fe SAs/NHCSSs is coordinated with four N atoms, forming a typical Fe_1N_4 structure.

To evaluate the catalytic performance of Fe SAs/NHCSSs, we performed the hydrogenation of nitrobenzene at $40 \text{ }^\circ\text{C}$ for 6 h. The Fe nanoparticles loaded on N doped hollow carbon (Fe NPs/NHCSSs) and N doped hollow carbon (NHCSSs) were used as reference catalysts. The dispersed Fe nanoparticles on Fe NPs/NHCSSs were verified by TEM, XRD and XPS measurements (ESI, Fig. S10–13†). As shown in Fig. 6a, nitrobenzene rarely converted into aminobenzene without a catalyst. Additionally, Fe NPs/NHCSSs and NHCSSs exhibited poor catalytic activity with 26% and 10% conversions, respectively. In contrast, Fe

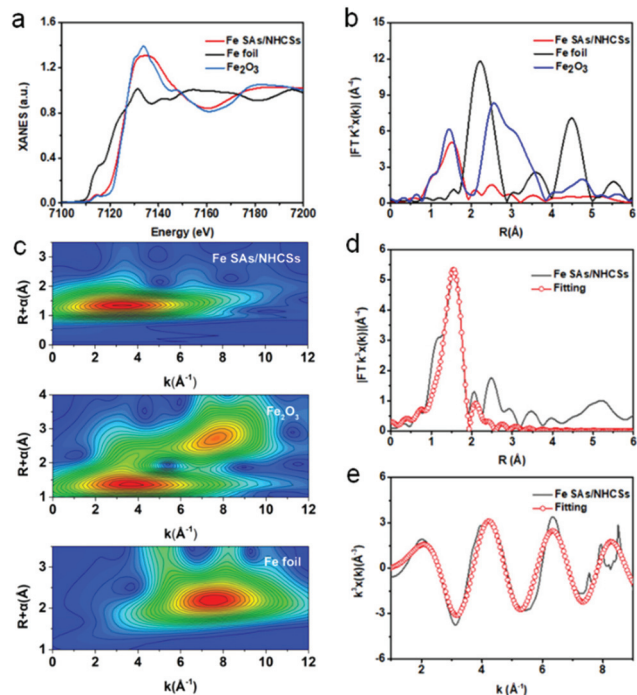


Fig. 5 (a) Fe K-edge XANES spectra of Fe SAs/NHCSSs, Fe foil, and Fe_2O_3 . (b) Fourier transform (FT) of Fe K-edge XANES spectra of Fe SAs/NHCSSs, Fe foil, and Fe_2O_3 . (c) Wavelet transform (WT) plots of Fe SAs/NHCSSs, Fe foil, and Fe_2O_3 . (d) The corresponding EXAFS fitting curve of Fe SAs/NHCSSs in the R space. (e) The EXAFS fitting curves of Fe SAs/NHCSSs in the k space.

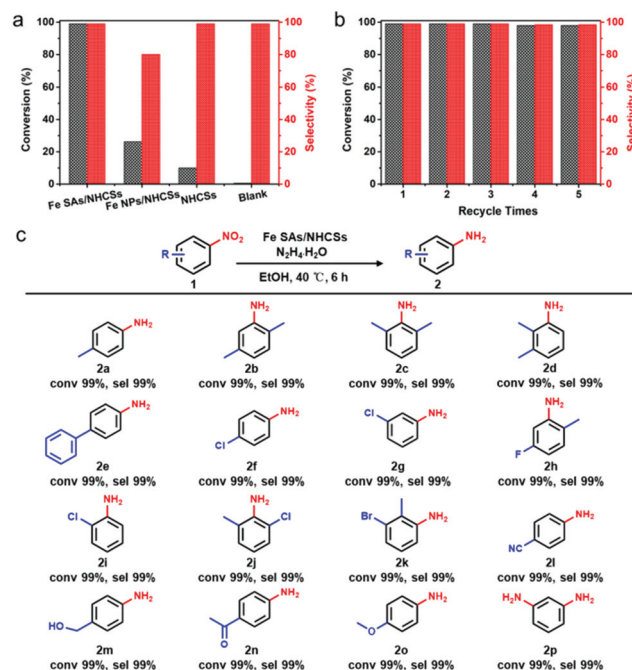


Fig. 6 (a) The catalytic performance of Fe SAs/NHCSS, Fe NPs/NHCSS, and NHCSS catalysts. (b) Recycling test of the Fe SAs/NHCSS catalyst. (c) Hydrogenation of the functionalized nitro-compounds by Fe SAs/NHCSSs.

SAs/NHCSs achieved a remarkable conversion of 99% with a selectivity to aminobenzene of 99%, which was higher than those of Fe NPs/NHCSs (ESI, Table S5†) and comparable to those of the reported catalysts (ESI, Table S6†). The kinetic analysis indicated that the hydrogenation of nitrobenzene over Fe SAs/NHCSs obeyed the first order kinetics (ESI, Fig. S14†). Fig. 6b shows the stability of the Fe SAs/NHCSs for the catalytic hydrogenation of nitrobenzene. Both the conversion and the selectivity of Fe SAs/NHCSs exhibited negligible decay after 5 cycles, demonstrating high stability. The Fe SAs/NHCSs after the stability test were characterized by HRTEM, elemental mapping, XRD and XPS (ESI, Fig. S15–17†). All results demonstrated the absence of Fe nanoparticles or clusters, which indicated that the Fe single atoms in Fe SAs/NHCSs hardly aggregated during the reusability tests. Consequently, Fe SAs/NHCSs served as robust catalysts for the highly efficient hydrogenation of nitrobenzene to aniline. Moreover, we performed the hydrogenation of nitroaromatic compounds with different substituents to study the hydrogenation scope of Fe SAs/NHCSs (Fig. 6c), and found that the Fe SAs/NHCS catalyst exhibits high activity and selectivity in the hydrogenation of all of the investigated nitroarenes. The results further confirm the high catalytic performance of the as-obtained Fe SAs/NHCS catalyst.

Conclusions

In this study, DFT calculations were used to predict the catalytic activity of the Fe SA catalyst in the hydrogenation of nitrobenzene to aniline. The results revealed that the isolated Fe atom on the support can weaken the adsorption of nitrobenzene on the catalyst surface, thus ensuring the appropriate adsorption energy of the reactants on the surface of the catalysts needed for an efficient catalytic process. Moreover, compared with the Fe NP catalyst, the activation barriers for the hydrogenation reaction on the Fe SA catalyst were much lower, which significantly increased the reaction rate. To validate the theory, Fe SAs/NHCSs were synthesized and the catalytic performance for the hydrogenation of nitrobenzene was performed. The experimental results were in good agreement with the theoretical calculations, since Fe SAs/NHCSs achieved a conversion of 99% with a selectivity of 99%, performance exceeding that of the Fe NPs/NHCSs. Our finding provides a new insight for the rational design of catalytic systems at the atomic level.

Conflicts of interest

The authors declare no conflict of interest.

Acknowledgements

This work was supported by the National Natural Science Foundation of China (21971002), the Natural Science

Foundation of Anhui province (1908085QB45, 2008085QB81, and 2008085QA33) and the Education Department of Anhui Province Foundation (KJ2019A0503). The calculations in this paper have been done using the supercomputing system of the National Supercomputing Center in Changsha. The authors thank BL1W1B in the Beijing Synchrotron Radiation Facility (BSRF) for help with characterization.

Notes and references

- 1 S. F. Cai, H. H. Duan, H. P. Rong, D. S. Wang, L. S. Li, W. He and Y. D. Li, *ACS Catal.*, 2013, **3**, 608–612.
- 2 H. S. Wilkinson, G. J. Tanoury, S. A. Wald and C. H. Senanayake, *Tetrahedron Lett.*, 2001, **42**, 167–170.
- 3 V. Pandarus, R. Ciriminna, F. Beland and M. Pagliarob, *Adv. Synth. Catal.*, 2011, **353**, 1306–1316.
- 4 H. H. Duan, D. S. Wang, Y. Kou and Y. D. Li, *Chem. Commun.*, 2013, **49**, 303–305.
- 5 R. Dey, N. Mukherjee, S. Ahammed and B. C. Ranu, *Chem. Commun.*, 2012, **48**, 7982–7984.
- 6 J. J. Mao, W. X. Chen, W. M. Sun, Z. Chen, J. J. Pei, D. S. He, C. L. Lv, D. S. Wang and Y. D. Li, *Angew. Chem., Int. Ed.*, 2017, **56**, 11971–11975.
- 7 A. Corma and P. Serna, *Science*, 2006, **313**, 332–334.
- 8 B. H. Wu, H. Q. Huang, J. Yang, N. F. Zheng and G. Fu, *Angew. Chem., Int. Ed.*, 2012, **51**, 3440–3443.
- 9 M. T. Zhao, K. Yuan, Y. Wang, G. D. Li, J. Guo, L. Gu, W. P. Hu, H. J. Zhao and Z. Y. Tang, *Nature*, 2016, **539**, 76–80.
- 10 Y. E. Wu, D. S. Wang, Z. Q. Niu, P. C. Chen, G. Zhou and Y. D. Li, *Angew. Chem., Int. Ed.*, 2012, **51**, 12524–12528.
- 11 L. Wang, E. J. Guan, J. Zhang, J. H. Yang, Y. H. Zhu, Y. Han, M. Yang, C. Cen, G. Fu, B. C. Gates and F. S. Xiao, *Nat. Commun.*, 2018, **9**, 1362.
- 12 W. J. Ma, J. J. Mao, X. T. Yang, C. Pan, W. X. Chen, M. Wang, P. Yu, L. Q. Mao and Y. D. Li, *Chem. Commun.*, 2019, **55**, 159–162.
- 13 J. J. Mao, C. T. He, J. J. Pei, W. X. Chen, D. S. He, Y. Q. He, Z. B. Zhuang, C. Chen, Q. Peng, D. S. Wang and Y. D. Li, *Nat. Commun.*, 2018, **9**, 4958.
- 14 H. F. Hou, J. J. Mao, Y. H. Han, F. Wu, M. N. Zhang, D. S. Wang, L. Q. Mao and Y. D. Li, *Sci. China: Chem.*, 2019, **62**, 1720–1724.
- 15 J. J. Mao, C. T. He, J. J. Pei, Y. Liu, J. Li, W. X. Chen, D. S. He, D. S. Wang and Y. D. Li, *Nano Lett.*, 2020, **20**, 3442–3448.
- 16 M. Zhou, Y. Jiang, G. Wang, W. J. Wu, W. X. Chen, P. Yu, Y. Q. Lin, J. J. Mao and L. Q. Mao, *Nat. Commun.*, 2020, **11**, 3188.
- 17 J. J. Mao, J. S. Yin, J. J. Pei, D. S. Wang and Y. D. Li, *Nano Today*, 2020, **34**, 100917.
- 18 W. J. Wu, Y. Liu, D. Liu, W. X. Chen, Z. Y. Song, X. M. Wang, Y. M. Zheng, N. Lu, C. X. Wang, J. J. Mao and Y. D. Li, *Nano Res.*, 2021, **14**, 998–1003.

- 19 G. Wang, C. T. He, R. Huang, J. J. Mao, D. S. Wang and Y. D. Li, *J. Am. Chem. Soc.*, 2020, **142**, 19339–19345.
- 20 H. B. Yang, S. F. Hung, S. Liu, K. D. Yuan, S. Miao, L. P. Zhang, X. Huang, H. Y. Wang, W. Z. Cai, R. Chen, J. J. Gao, X. F. Yang, W. Chen, Y. Q. Huang, H. M. Chen, C. M. Li, T. Zhang and B. Liu, *Nat. Energy*, 2018, **3**, 140–147.
- 21 P. Q. Yin, T. Yao, Y. Wu, L. P. Zheng, Y. Lin, W. Liu, H. X. Ju, J. F. Zhu, X. Hong, Z. X. Deng, G. Zhou, S. Q. Wei and Y. D. Li, *Angew. Chem., Int. Ed.*, 2016, **55**, 10800–10805.
- 22 Y. Liu, G. X. Zhu, A. Li, J. J. Pei, Y. M. Zheng, W. X. Chen, J. Ding, W. J. Wu, T. Wang, D. S. Wang and J. J. Mao, *Nano Energy*, 2021, **83**, 105799.
- 23 W. Wan, X. F. Liu, Y. C. Li, R. H. Yu, L. R. Zheng, W. S. Yan, H. Wang, M. Xu and J. L. Shui, *Nat. Catal.*, 2019, **2**, 259–268.
- 24 L. Jiao and H. L. Jiang, *Chem*, 2019, **5**, 786–804.
- 25 S. B. Tang, Q. Dang, T. Y. Liu, S. Y. Zhang, Z. G. Zhou, X. K. Li, X. J. Wang, E. Sharman, Y. Luo and J. Jiang, *J. Am. Chem. Soc.*, 2020, **142**, 19308–19315.
- 26 J. Z. Li, M. J. Chen, D. A. Cullen, S. Hwang, M. Y. Wang, B. Y. Li, K. X. Liu, S. Karakalos, M. Lucero, H. G. Zhang, C. Lei, H. Xu, G. E. Sterbinsky, Z. X. Feng, D. Su, K. L. More, G. F. Wang, Z. B. Wang and G. Wu, *Nat. Catal.*, 2018, **1**, 935–945.
- 27 K. Jiang, B. Y. Liu, M. Luo, S. C. Ning, M. Peng, Y. Zhao, Y. R. Lu, T. S. Chan, F. M. F. de Groot and Y. Tan, *Nat. Commun.*, 2019, **10**, 1743.
- 28 Z. Q. Zhang, Y. G. Chen, L. Q. Zhou, C. Chen, Z. Han, B. S. Zhang, Q. Wu, L. J. Yang, L. Y. Du, Y. F. Bu, P. Wang, X. Z. Wang, H. Yang and Z. Hu, *Nat. Commun.*, 2019, **10**, 1657.
- 29 W. H. Zhong, Y. Qiu, H. J. Shen, X. J. Wang, J. Y. Yuan, C. Y. Jia, S. W. Bi and J. Jiang, *J. Am. Chem. Soc.*, 2021, **143**, 4405–4413.
- 30 L. Yang, D. J. Cheng, H. X. Xu, X. F. Zeng, X. Wan, J. L. Shui, Z. H. Xiang and D. P. Cao, *Proc. Natl. Acad. Sci. U. S. A.*, 2018, **115**, 6626–6631.
- 31 P. Y. Xin, J. Li, Y. Xiong, X. Wu, J. C. Dong, W. X. Chen, Y. Wang, L. Gu, J. Luo, H. P. Rong, C. Chen, Q. Peng, D. S. Wang and Y. D. Li, *Angew. Chem., Int. Ed.*, 2018, **57**, 4642–4646.
- 32 Z. C. Zhang, Q. Kang, D. S. Wang and Y. D. Li, *Nano Res.*, 2020, **13**, 1856–1866.
- 33 J. Zhang, C. Y. Zheng, M. L. Zhang, Y. J. Qiu, Q. Xu, W. C. Cheong, W. X. Chen, L. R. Zheng, L. Gu, Z. P. Hu, D. S. Wang and Y. D. Li, *Nano Res.*, 2020, **13**, 3082–3087.
- 34 N. Q. Zhang, C. L. Ye, H. Yan, D. S. Wang and Y. D. Li, *Nano Res.*, 2020, **13**, 3165–3182.
- 35 T. T. Sun, L. B. Xu, D. S. Wang and Y. D. Li, *Nano Res.*, 2019, **12**, 2067–2080.
- 36 J. R. Yang, W. H. Li, D. S. Wang and Y. D. Li, *Small Struct.*, 2021, **2**, 2000051.
- 37 X. Y. Li, H. P. Rong, J. T. Zhang, D. S. Wang and Y. D. Li, *Nano Res.*, 2020, **13**, 1842–1855.
- 38 T. W. He, C. M. Zhang, L. Zhang and A. J. Du, *Nano Res.*, 2019, **12**, 1817–1823.
- 39 S. Wang, Y. J. Liu and J. X. Zhao, *Phys. Chem. Chem. Phys.*, 2020, **22**, 17639–17645.
- 40 M. L. Zhang, Y. G. Wang, W. X. Chen, J. C. Dong, L. R. Zheng, J. Luo, J. W. Wan, S. B. Tian, W. C. Cheong, D. S. Wang and Y. D. Li, *J. Am. Chem. Soc.*, 2017, **139**, 10976–10979.